Maximizing the efficiency of intrapulse difference frequency generation by pulse shaping and recycling

Quentin Bournet, Mindaugas Jonusas, Florent Guichard, Michele Natile, Yoann Zaouter, Manuel Joffre, Adeline Bonvalet, Fréderic Druon, Marc Hanna, Patrick Georges

Maximizing the efficiency of intrapulse difference frequency generation by pulse shaping and recycling

Quentin Bournet[1,2], Mindaugas Jonusas[3], Florent Guichard[2], Michele Natile[2], Yoann Zaouter[2], Manuel Joffre[3], Adeline Bonvalet[3], Fréderic Druon[1*], Marc Hanna[1], Patrick Georges[1]

[1*]Université Paris-Saclay, Institut d'Optique Graduate School, CNRS, Laboratoire Charles Fabry, Palaiseau, 91127, France.
[2]Amplitude, 11 Avenue de Canteranne, Cité de la Photonique France, Pessac, 33600, France.
[3]Laboratoire d'Optique et Biosciences, Ecole Polytechnique, CNRS, INSERM, Institut Polytechnique de Paris, Palaiseau, 91128, France.

*Corresponding author(s). E-mail(s): frederic.druon@institutoptique.fr;

Abstract

Intrapulse Difference Frequency Generation (iDFG) is an interesting technique for generating femtosecond pulses in the Mid-Infrared (MIR) range with unique properties such as robust Carrier-Envelope Phase (CEP) stability. However, its efficiency is low compared to other techniques. In this paper, we describe an iDFG system operating within the 4 to 10 µm range that features an original architecture to enhance efficiency. First, we introduce an interesting technique on the generation process. This approach involves polarization and spectral phase shaping techniques on the driving pulse to maximize the number of photons enrolled in the process. Second, we demonstrate that the polarization shaping allows further enhancement of efficiency by recycling the iDFG signal to pump a subsequent optical parametric amplification (OPA) stage. These two concepts and the associated parameters optimization are described into details, and supported by experimental results. Combined with a high-power Yb-fiber-based pump laser, these techniques allow to achieve record efficiencies, and generate µJ-level, few-cycle, tunable, CEP-stable pulses in the MIR at repetition rates above 100 kHz.

Keywords: Ultrafast lasers, Mid-Infrared lasers, Nonlinear optics

1 Introduction

A significant effort is currently underway within the laser research community to actively advance the development of high repetition rate ultrafast sources in the mid-infrared (MIR) range. These sources play a crucial role in a growing range of applications, including high-field physics in both bulk and nanostructured solids [1, 2], field-resolved spectroscopy [3], and two-dimensional infrared (2DIR) spectroscopy [4–6]. Particularly noteworthy is the use of 2DIR spectroscopy for studying changes in the conformation of proteins, which opens up possibilities for investigating the dynamics of biologically important molecules. For these applications, a large number of 2DIR spectra must be acquired employing ultrashort pulses with high energy in the mid-infrared range. Recent research endeavors in the field of mid-infrared sources have concentrated on the combination of diode-pumped laser sources with high repetition rates and optical parametric amplification (OPA) systems that utilize supercontinuum seeding. These systems exhibit varying levels of complexity and often incorporate an additional stage of difference frequency generation (DFG). Notably, recent studies have indicated that a repetition rate of around 100 kHz [7–9] offers a favorable balance between rapid data averaging and the capability to capture individual spectra for each laser pulse. However, these sources are relatively inefficient, as the ratio between the energy in the mid-infrared range and the total energy of the pump is ranging from 0.2% to 2.6% at wavelengths of 7-8 μm [10–16]. Another technique for MIR generation involves the implementation of intra-pulse difference frequency generation (iDFG) utilizing a sufficiently short pump pulse [17, 18]. As shown in the schematic Fig. 1, in this method, if the spectrum of the incoming pump pulse encompasses a frequency range that exceeds the desired optical frequency in the mid-infrared (MIR), it becomes feasible to create a frequency difference between the extreme wavelengths within the pump spectrum. However , to reach the MIR region, a nonlinear compression stage (Fig. 1(b)) is often necessary.

On the other hand, iDFG is very attractive with a straightforward implementation, inherent spatial-temporal overlap. Nevertheless, the conversion efficiencies associated with this technique generally tend to be lower than those of OPA-based sources (<0.5%, typically around 0.1% at wavelengths ranging from 6 to 10 μm) [3, 19–22]. This arises from the fact that only a fraction of the pump photons contributes to the interaction, both in terms of spectral content and polarization state.

2 The bottleneck of iDFG efficiency

Recent instances of iDFG systems have emerged, capitalizing on the high-repetition-rate 1-μm wavelength pump sources that benefit from mature ytterbium laser technology. However, as shown in Fig. 2, with 1-μm pumping, the efficiency rarely exceeds 0.1 %. Different solutions to overcome this technological bottleneck have been studied. One can increase the wavelength of the pump laser, losing the advantages of the ytterbium laser technology. Indeed, for identical quantum yields, the efficiencies increase with the pump wavelength. For example, in the case of a generation at 8 μm, a quantum yield of 100% corresponds to a maximum theoretical efficiency of 12.5%, 25% and 37% for a pump at 1, 2 or 3 μm respectively. A second way consists

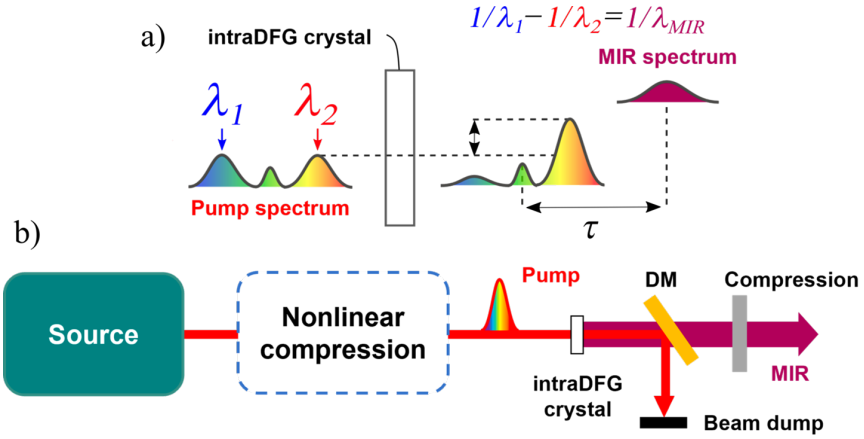

Fig. 1 (a) Sketch of the iDFG process in the spectro-temporal domain. After the crystal, the pump (resp. signal) part of the driving spectrum centered at λ_1 (resp. λ_2) is depleted (resp. amplified), and a MIR pulse is generated. The MIR/driving pulses are temporally delayed by τ due to the GVM. (b) Schematic of an iDFG experimental setup. If the spectrum of the pump source is not broad enough, a nonlinear compression scheme must be added prior to the generation stage. DM: dichroic mirror.

in developing highly efficient iDFG-based systems, i.e. maximizing the MIR energies produced, for a given pump. Ideally, this last possibility can be combined with longer wavelength pumps. Fig. 2 summarizes some significant results for MIR generation in the 4-20 μm spectral range via iDFG, including the amplified architecture from [23]. We have grouped these sources into three main categories. The first one (blue circles in Fig. 2 (a) and (b)) concerns systems using NIR pumps at 1 μm. The second (green squares) refers to pumps between 1.5 and 2 μm, while the last one (red stars) corresponds to MWIR pumps from 2.5 to 3 μm. From Fig. 2 (a), repetition rates regimes are typically centered around (i) the kHz, (ii) few hundreds of kHz and (iii) up to 100 MHz. It is obvious that due to the limited average powers available, energies decrease as the repetition rates increase. The ideal scenario for a fixed repetition rate is therefore to extract the highest possible energy to increase the generated average power. Although the global performances of architectures pumped around 2 to 3 μm may appear to be similar to those pumped at 1 μm, the advantage of pumping at longer wavelengths is highlighted when looking at the global optical-to-optical efficiencies (Fig. 2 (b)): about one order of magnitude separates each pump category. In particular, the highest efficiencies are obtained for pumps around 3 μm pumping, which can reach several % levels. The spectral bandwidths obtained are presented in Fig. 2 (c). Depending on the crystal, a very broad range of MIR wavelengths is covered, roughly ranging from 4 to 18 μm. In particular, although pumped at lower intensities than LGS, GaSe crystals allow for the broadest bandwidths to be covered because they are not limited by absorption around 12 μm. IDFG allows then the production of extremely broad spectra.

In this paper, we demonstrate an iDFG architecture to address the efficiency issues of this technique. We combine two ideas: the first one concerns the generation process, the second one concerns an additional simple amplifier. Concerning the generation,

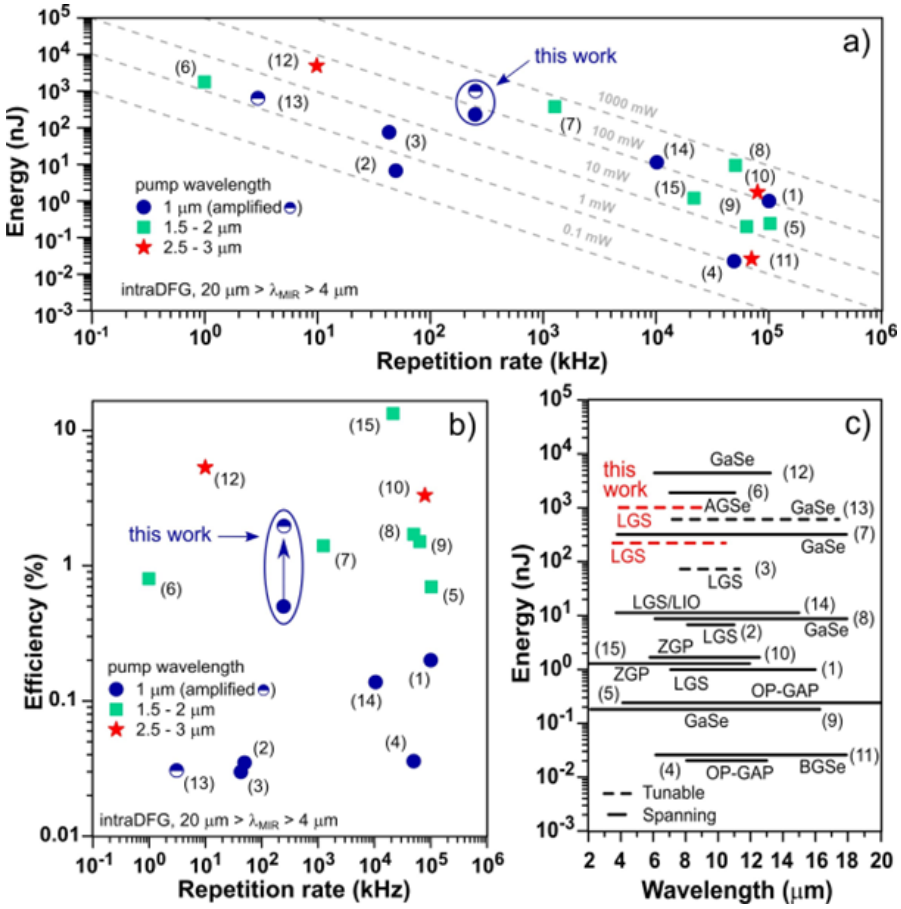

Fig. 2 State of the art of DFG-based technologies. (a) Energies for setups pumped at 1 μm (blue), 1.5-2 μm (green) and 2.5-3 μm (red), as a function of the repetition rate. (b) Optical-to-optical efficiencies following the same color code as a function of the repetition rate. (c) Energies and spectral bandwidths. The references are the following ones: (1)[19]; (2)[14]; (3) [24]; (4)[25]; (5)[26]; (6)[27]; (7)[28] (8)[29]; (9)[24]; (10) [30]; (11)[31]; (12)[32]; (13) [23]; (14)[33], [34].

the concept is based on the simple addition of carefully designed plates of birefringent and isotropic materials along the beam propagation. This implementation results in several key features: (i) the polarization states of the incoming spectral components are selectively rotated on the relevant orthogonal axes of the crystal to maximize the nonlinear interaction efficiency. The latter is further increased by (ii) optimizing the chirp of the incoming pulses onto the crystal and (iii) finely adjusting the delay between the spectral components involved in the 3 -wave mixing process. This approach allows to achieve efficiencies comparable to those of 1 μm-pumped OPA-based setups and close to the ones obtained with iDFG architectures pumped at 2 μm. In addition, this unique set of parameters allows us to (iv) amplify the CEP-stable MIR pulses in a subsequent OPA stage pumped by the recycled long-wavelength photons amplified in the iDFG stage. Another advantage of this architecture, as we will see, is that it

can be optimized in separate lines for signal and pump or all inline, without requiring alignment for both spatial and temporal overlaps. Indeed, this iDFG architecture is especially adapted to post-amplification in OPA stage and in particular, for inline amplification. This post amplification makes possible to reach even higher efficiencies, one order of magnitude above the highest one reported when pumped at 1 μm.

3 Efficient high-repetition rate, 1 μm source for iDFG

In this section, we detail the properties of the pulses used to drive the MIR generation. The primary laser source is an Yb-doped-fiber amplifier that generates 200 μJ pulses at a central wavelength of 1030 nm, at 250 kHz for an average power of 50 W. These pulses have a duration of 260 fs and the beam exhibits a quality factor (M2) of 1.3 x 1.2 at the laser output. To broaden the pulse spectrum, a highly efficient dual-stage nonlinear compression setup, similar to the one described in [35], is employed. The initial nonlinear compression stage employs a gas-filled multipass cell and chirped mirrors,(from Laser Quantum), reducing the pulse duration to 43 fs. Subsequently, the pulses pass through a second nonlinear compression stage that relies on a 350 μm diameter gas-filled 1 m-long hollow-core-fiber and subsequent chirped mirrors. In this stage, the pulse width is further compressed to sub 10 fs, as shown in Fig. 3, and the total average power is reduced to 34.5 W. The total transmission of the dual-stage compression scheme is 70% for a total compression factor of 41.

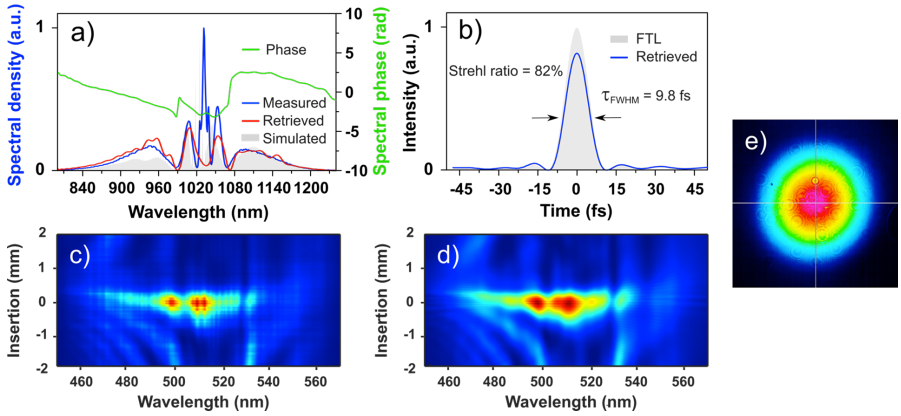

Fig. 3 (a) Simulated (gray filled curve), retrieved (red curve) and measured (blue curve) spectra at the output of the dual-stage post-compression system. (b) FTL (gray filled curve) and retrieved (blue curve) compressed pulse. The measured and retrieved DSCAN traces are shown in (c) and (d), respectively. (e) Collimated output mode of the hollow core fiber.

4 iDFG with pump-polarization optimization

The pulse spectrum is now broad enough to pump the iDFG stage. In the following, these pulses are referred to as driving pulses. To prevent excessive intensity on the iDFG crystal, only a portion of the total output power is used, accomplished by employing a beam splitter (Fig. 4). The second line pulses can be used as electro-optical sampling (EOS) gate. In that case, only 10 % of the energy is needed. A part of the remaining pump energy can also be used for chirped-pulse upconversion [36] after suitable stretching. At the output of the crystal, we incorporate a dichroic mirror to filter out the NIR pulses, and a coated ZnSe lens is employed to collimate the MIR beam. To temporally compress the pulses, we utilize a coated germanium plate.

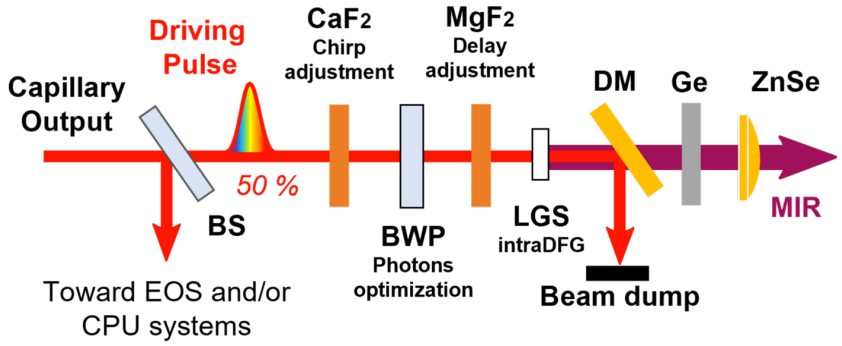

Fig. 4 Schematic of the iDFG experimental setups. BS: beam-splitter; BWP: bichromatic waveplate; DM: dichroic mirror (HR for $\lambda < 2$ μm, HT for $\lambda > 2$ μm). (EOS: electro-optical sampling CPU: chirped-pulse upconversion. The manufacturers are, for the BWP plate Crylight Photonics, for the CaF_2 and MgF_2 plates Altechna and for the LGS crystal Ascut.

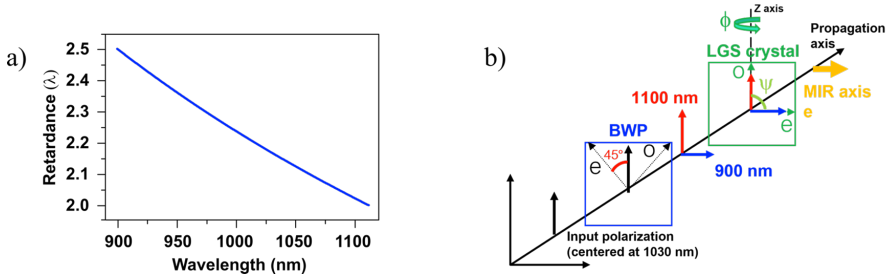

Fig. 5 (a) Retardance as a function of the wavelengths for a 255 μm-thick BWP. (b) Evolution of polarization states sketch along the propagation axis.

For iDFG, we use a LGS crystal anti-reflection coated for wavelengths in the range of 900 – 1100 nm (<1% reflectivity) and in the range of 4 - 8 μm (<4% reflectivity). In the experiments, we employed two different crystals, with thicknesses of 1 mm and 2 mm, respectively, and oriented in the XY plane at angles θ of 90° and ϕ of 44.1°. This

orientation corresponds to a type II phase matching configuration for our pump beam at 900 nm, which is polarized in the XY plane (referred to as extraordinary), and our signal beam at 1100 nm propagating along the Z direction (referred to as ordinary). The idler beam in the mid-infrared is polarized along the e (extraordinary) direction. To adapt the beam size, we employ an afocal system consisting of two curved mirrors, which ensures that the beam is directed onto the crystal without focusing. The total average power incident on the LGS crystal is 19.7 W (79 μJ) with a $1/e^2$ diameter of 3.6 mm, corresponding to an estimated peak intensity of 150 GW/cm^2. This intensity level is in line with other LGS-based systems [19, 37]. The iDFG process requires orthogonal polarization states for the pump and signal that are two extremes of the spectral components. Usually, one aligns the input polarization on the nonlinear crystal at a 45-degree angle with respect to the principal axes orientation [18, 28, 38]. This arrangement evenly distributes the entire spectrum across the crystal axes, resulting in the waste of half of the available photons. As illustrated in Fig. 5, a more effective solution involves the use of a multi-order wave plate. This simple device serves to separate all pump and signal photons onto the e and o (ordinary) axes of the LGS crystal, respectively. Consequently, this approach effectively doubles the number of pump and signal photons participating in the interaction process [39].

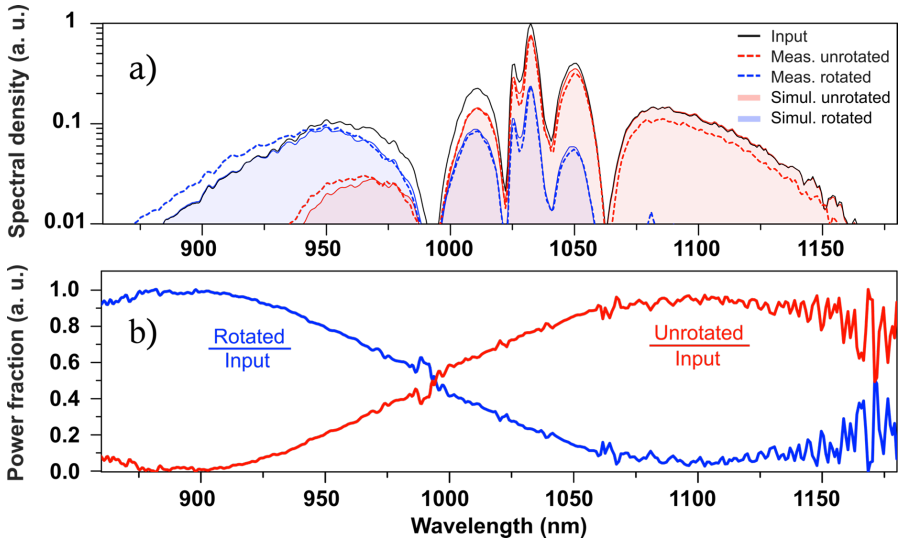

Fig. 6 (a) Experimental spectrum at the BWP input (black curve). Measured (red dashed lines) and calculated (red filled curve) unrotated spectra after the BWP. Measured (blue dashed lines) and calculated (blue filled curve) rotated spectra after the BWP. (b) Measured power fraction of rotated (blue curve) and unrotated (red curve) polarizations as a function of wavelength.

The addition of the BWP makes it possible to introduce two cross-polarized pulses with very distinct spectral content, as shown in Fig. 6. However, since the pump and the signal come from the same initial pulse, their own chirp as well as their relative time delay are intrinsically linked to the characteristics of the latter. The temporal aspects in an iDFG architecture are therefore more complex to manipulate than traditional

OPA schemes where independent pump and signal lines are used. Yet, for ultrashort pulses as it is specifically the case in iDFG, nonlinear gains, spectral bandwidths and durations of the generated MIR pulses highly depend on the temporal aspects of the propagation. In light of simulations that are supported by experimental results, we endeavor in the following to describe the temporal aspects of such an interaction, in order to maximize the overall efficiency. In Fig. 4, one can notice that CaF_2 and birefringent MgF_2 plates have been introduced before reaching the LGS crystal. First, let us see how the chirp of the driving pulses affects the MIR power. A certain thickness of CaF_2, presenting a normal dispersion of $\sim 19\ fs^2/mm$ around 1 μm, is introduced in the setup. This adjustment slightly tunes the temporal compression of the driving pulse. Simultaneously, its duration is measured before the BWP using the DSCAN system [40], and the MIR power is monitored. We performed this measurement at the extrema of the MIR tunability range (at 4.7 and 8 μm). Results are shown in Fig. 7. The optimal compression is identified when adding 8 mm of CaF_2 in addition to the Group Delay Dispersion (GDD) induced by the chirped mirrors. At this particular point, the pulse duration is the smallest, and the temporal intensity is maximal at the input of the crystal. In the graph, this position is set to 0 mm, and a negative quantity of CaF_2 means that it has been removed and corresponds to a negatively chirped pulse. Interestingly, the highest MIR power is not reached at the optimal compression of the driving pulse for both central wavelengths. More surprisingly, it is not reached for the same chirp configuration. At 8 μm, the maximum corresponds to 1 mm of CaF_2 and a 15 fs-long pulse, while the 4.7 μm power is still increasing after -3 mm, corresponding to a pulse duration of more than 25 fs.

Numerical simulations are performed to explain this behavior. The code is run for different CaF_2 thicknesses, for two phase-matching conditions, at 4.7 and 8 μm, and the efficiency of the nonlinear process is calculated. The code is based on a 1D description of the pump, signal and idler optical fields E(z,t) propagating along the eigenaxes of the various materials, using a model similar to that presented in [41]. The spatial aspect of the propagation is taken into account by repeating 1D simulations with intensities varying across the profile. This allows to estimate efficiencies more realistically. Results are shown in Fig. 8, and the measurements are reported on the same CaF_2 range. It is in good agreement with the measurements, although it is slightly shifted by about 1 mm of CaF_2, probably due to the spectral phase set to zero in the simulation. For the same reason, the simulation does not account for possible temporal pedestals and fails to produce the weak generation observed for negative values of CaF_2. At both MIR central wavelengths, the MIR power follows a bell-shaped curve shifting as the central wavelength changes. This optimal efficiency is due to a better temporal overlap between the pump and signal interacting wavelengths of the different pulses that change with the chirp adjustment. On the left panel, at 4.7 μm, optimal MIR power is reached at 4 mm and -3 mm for the measured and simulated cases, respectively. On the right panel, at 8 μm, optimal MIR power is reached at -1 mm for both the measured and simulated cases. Three different behaviors occur in the NL crystal: (i) at optimal compression (green zone in Fig. 8), (ii) at optimal 4.7 μm MIR power (red zone), and (iii) at -8 mm of CaF_2 corresponding to a highly negatively chirped input pulse (blue zone).

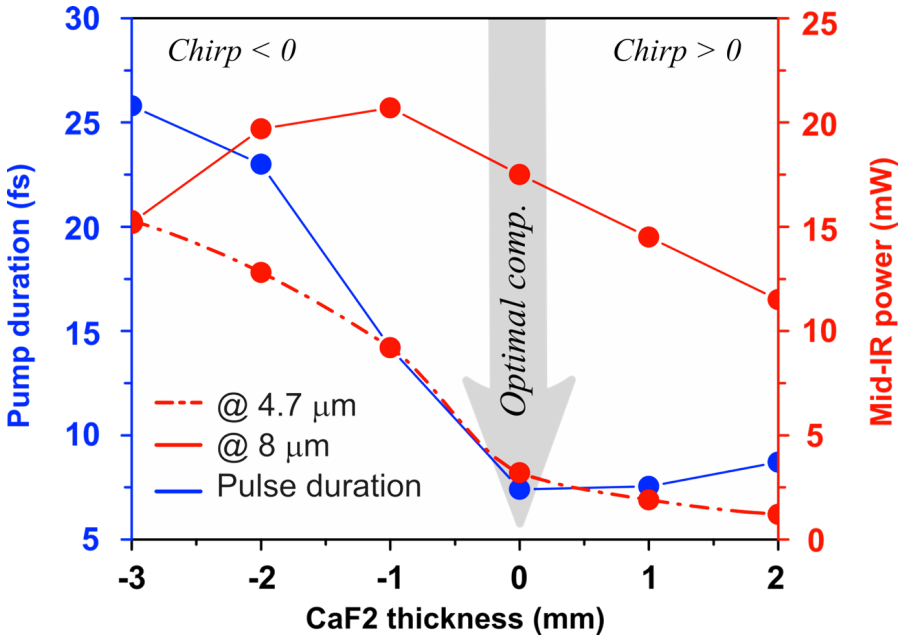

Fig. 7 Driving pulse duration (blue curve) measured with a DSCAN system at the input of the crystal without the BWP, and MIR average powers generated at the central wavelengths of 4.7 μm (red dashed lines) and 8 μm (red curve) for a 1 mm-thick LGS crystal, as a function of the CaF_2 thickness. Optical compression is set at 0 mm in the graphs so that negative values correspond to a negatively chirped pulse.

The optimization of the chirp will impose consequences on the group delay in the LGS between the bluest and reddest components of the spectrum. A decoupling between chirp and delay can be used to introduce an additional degree of freedom in the all-inline intra-DFG architecture, such as in a classic OPA architecture with separate pump and signal lines. In our case, we use MgF_2 (Fig. 4), presenting a strong birefringence and a weak GVD, of the order of 11 fs^2/mm around 1 μm. The configuration is as follows: the driving pulses are highly negatively chirped at the entrance of the crystal (approximately 35 fs) by removing 8 mm of CaF_2, representing a GDD of -150 fs^2. After the BWP, 800 μm of MgF_2, calculated from the simulations, are inserted to compensate for the delay introduced by the chirp. Fig. 9 shows the results for the central wavelength of 8 μm. In this specific configuration, in addition to a maximized intensity along the propagation, the pulse delay is close to 0. The gain in this configuration is multiplied by a factor of 1.3 in the simulations and by a factor of 1.7 in the experiments for a 1 mm-thick crystal. Note that in the measurements, input power is considered with no losses due to reflection on the uncoated plates, so this value can be increased using coated elements.

These two additional degrees of freedom allow to optimize the MIR generation and can be adjusted versus the MIR wavelength in our enhanced iDFG where the number of photons enrolled in the NL interaction has been optimized. Fig. 10 (a) summarizes all the above-mentioned measured and simulated energies. By combining the BWP

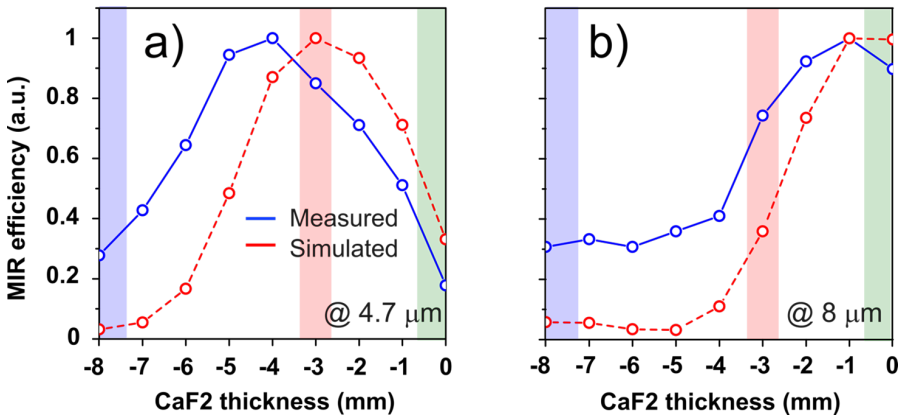

Fig. 8 Intra-DFG theoretical (red dashed lines) and measured (blue curves) efficiencies at a central wavelength of 4.7 μm (a) and 8 μm (b) as a function of the CaF_2 thickness for a 1 mm-thick LGS crystal. The optimal compression is set at 0 mm of CaF_2. Each set of data is normalized with regard to its own maximum value.

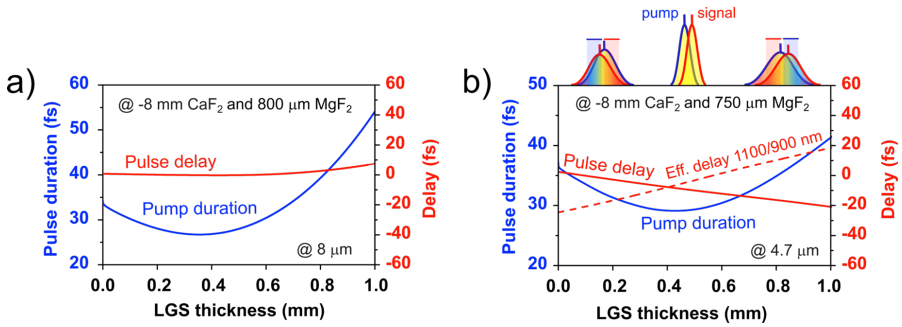

Fig. 9 Simulations of the pump pulse duration (blue curve), the pulse delay taken at the central frequencies of the pump and signal pulses, and the effective delay of the interacting components for the 8 μm (a) and the 4.7 μm (b) generation. They are plotted as a function of the LGS thickness.

with chirp and delay management plates for a 1 mm-thick LGS crystal (in our case, -8 mm of CaF_2 and 800 μm of MgF_2), the efficiency is increased by a factor of more than 4 at the central wavelength of 8 μm. Although the chirp and delay management configuration does not increase the obtained energies for shorter MIR wavelengths compared to chirp adjustment only, it eliminates the need to change the thickness of materials during frequency tunability of the generation, which was required in the latter configuration. In Fig. 10 (b), the measured energies in the chirp and delay configuration are compared at each MIR central wavelength to the ones obtained in a standard configuration without BWP and optimal compression. Energies increase as the wavelength decreases because the optimal compression favors generation at 8 μm. Table 1 summarizes the energies and associated efficiencies obtained different wavelengths. The measured spectra (OSA207C, Thorlabs) in the chirp adjustment only and chirp and delay management configurations are very similar (Fig. 10 (c)).

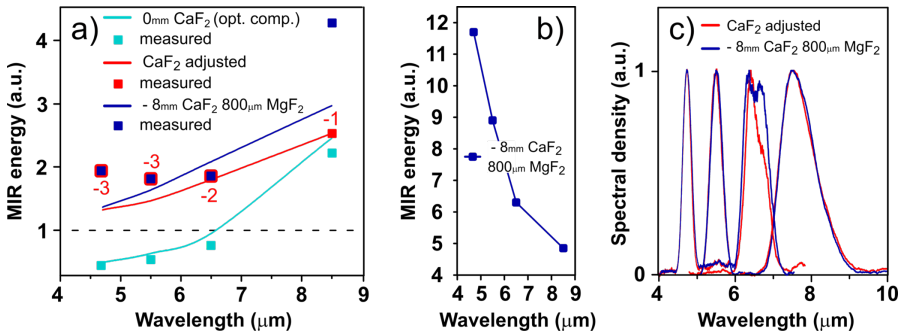

Fig. 10 (a) Simulated (solid lines) and measured (squares) energies of the optimal compression (0 mm CaF_2) (green), chirp-adjusted (red), and chirp-and-delay-management (blue) setup configurations. Energies are normalized to the highest one obtained with chirp adjustment without BWP at 8 μm (black dashed lines). The thicknesses of CaF_2 inserted at each central wavelength for the chirp adjustment configuration are displayed. (b) Chirp-and-delay-management configuration energies normalized to the standard iDFG at optimal compression without BWP at the same wavelength. (c) Measured spectrum tunability in the chirp-adjustment (red) and chirp-and-delay-management (blue) configurations.

Wavelength (μm)	Average power (mW)	Energy (nJ)	Efficiency (%)
4	5	20	0.05
4.7	17	68	0.15
5.5	15	60	0.14
6.5	12	48	0.12
7.5	18	72	0.16
8.5	18	72	0.17

Table 1 Measured mid-IR average powers and yields with 1 mm-thick LGS XY crystal at I=140 GW/cm^2 at the output of the iDFG stage.

For temporal characterization of the MIR, we use the Electro-Optic Sampling (EOS) technique. The EOS setup is built around a 30 µm-thick GaSe crystal (from EKSMA). Fig. 11 shows the measured (black) and deconvolved (blue) EOS traces corresponding to the MIR pulse generated using the 1 mm-thick type II LGS crystal at a central frequency of 8.6 μm. For deconvolution, the response function of the EOS system is obtained through 1D (z,t) simulations of the sum-frequency generation process in the 30 µm-thick GaSe crystal, with a gate function obtained from the DSCAN characterization of the few-cycle driving pulses at 1 µm. At this wavelength, the GDD introduced corresponds to -4000 fs^2 and 420 fs^2 for the LGS and the 1 mm-thick ZnSe dichroic mirror, respectively. Therefore, the total GDD that the MIR pulse experiences during propagation is approximately -3580 fs^2, which can be compensated by 7 mm of germanium (GVD = 510 fs^2/mm). This corresponds precisely to the thickness of the germanium windows crossed by the MIR beam for spatial recombination in the EOS, at an angle of 45°. Therefore, the retrieved spectral phase (green) is flat, showing that the pulses are temporally compressed. The corresponding pulse duration is 49 fs, close to the Fourier Transform Limited (FTL) one of 47.4 fs. It corresponds to 1.7 optical cycles at the central wavelength of 8.6 μm.

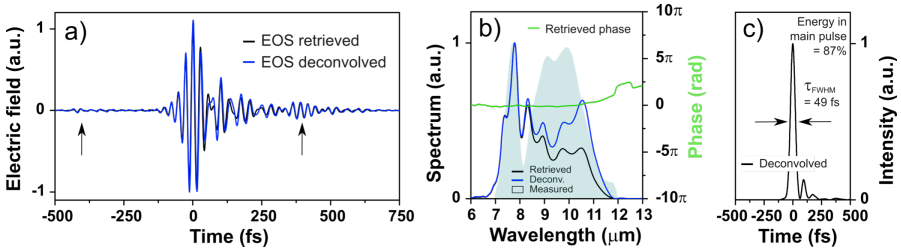

Fig. 11 (a) Raw (black curve) and deconvolved (blue curve) time-domain EOS traces for a 1 mm-thick crystal. The replicas are marked by black arrows. (b) Fourier transforms of the EOS time-domain traces and retrieved spectral phase (green curve). Spectrum measured with the Fourier Transform InfraRed FTIR spectrometer (gray filled curve). (c) Corresponding intensity profile in the time domain.

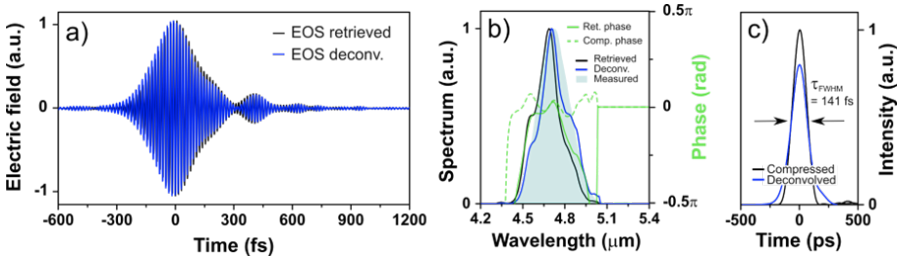

Fig. 12 (a) Raw (black curve) and deconvolved (blue curve) time-domain EOS traces for a 1 mm-thick crystal. (b) Fourier transforms of the EOS time-domain traces. The retrieved spectral phase (green curve) and the one corresponding to the compressed pulse (green dashed line) are also shown. Spectrum measured with the FTIR spectrometer (gray filled curve). (c) Corresponding intensity profiles in the time domain.

In the same point of view, Fig. 12 displays the EOS measurements for the 4.7 μm MIR pulse, with a corresponding pulse duration of 162 fs. Unlike the previous case, the LGS does not exhibit high GDD at this wavelength (-257 fs^2). As the ZnSe dichroic mirror only adds 56 fs^2, it is the germanium that introduces the highest dispersion (GVD = 915 fs^2/mm). The total dispersion induced by propagation is thus 6200 fs^2, resulting in a highly positive chirped pulse. To compress the pulse, 6.8 mm of germanium must be removed, which once again corresponds precisely to the thickness traversed in the Ge recombination window of the EOS setup. This is done in the code to estimate the pulse duration before the EOS device, resulting in a duration of 140 fs, very close to the FTL one of 132 fs.

In inter-pulse DFG architectures, the output pulse Carrier Envelope Phase (CEP) fluctuates over time due to variations in the relative optical path lengths between two separate beams. This necessitates an active feedback system to achieve a minimal fluctuation of 100-200 mrad [42, 43]. In comparison, iDFG offers a significant advantage in CEP stability because the interacting beams share a common path. We characterize the CEP stability by measuring one EOS trace every 10 seconds for 30 minutes. The 180 traces are shown in Fig. 13, showing a CEP stability of 120 mrad RMS without any active feedback system.

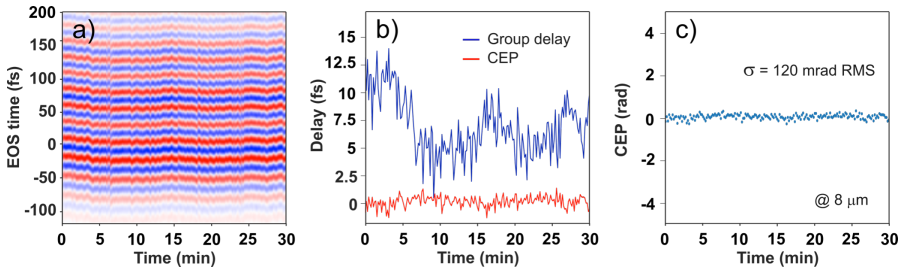

Fig. 13 (a) Color-coded raw EOS traces as a function of time. (b) Phase delay (orange curve) and group delay (blue curve) extracted from (a). (c) Standard deviation of the phase delay. Measurements are performed at the MIR central frequency of 8 μm.

In conclusion, the optimization of the polarization by employing a simple wave-plate capable of spectrally dependent polarization rotation, of the pulse duration by employing CaF_2 plate and of the pump-to-signal delay by employing MgF_2 plate, allows to demonstrate a significant increase in mid-infrared average power generated through iDFG by a factor of $\geq$2.5. With the inclusion of this wave plate (BWP), this "enhanced" iDFG allows efficiencies up to 0.16%, a notable improvement compared to the 0.07 % efficiency achieved without it (using a 1-mm-thick LGS crystal). Nevertheless, reaching the percent level remains an interesting objective to reach.

5 Post-amplification of iDFG pulses

Amplification of the MIR pulses recycling the remaining pump is an attractive way to improve the efficiency of the iDFG. We propose to use what was the signal in the iDFG process (1.03 μm $< \lambda <$ 1.15 μm) to serve as a pump in a subsequent OPA stage. Although the pump frequencies are depleted by the MIR generation at the output of the iDFG crystal, the signal frequencies are indeed amplified. In a standard architecture, this pump (iDFG signal) is separated and resynchronized with the MIR beam using a delay stage. Another possibility is to use the same concept in an all-inline configuration, where temporal synchronization is adjusted using a carefully selected birefringent material thickness [44]. The main concept presented in the following involves utilizing the increased number of signal photons to pump parametric amplification of MIR pulses in a second LGS crystal, later denoted as the OPA crystal. The type I (XZ plane) phase matching angle required for MIR amplification around 8 μm in the OPA crystal is 51.3°. Fig. 14 (a) shows the standard configuration, i.e., sending the driving pulse at 45° from the eigenaxes of the LGS crystals.

Unfortunately, the phase matching angle for amplification also corresponds to MIR generation via iDFG (at $\theta = 50.7°$). To avoid the latter, the BWP studied in the previous iDFG scheme can be used (see Fig. 14 (b)). Indeed, in that specific case, the signal photons are routed to the e-axis (belonging to the XZ plane) of the OPA crystal, thus preventing phase matching for the second generation. Note that we will keep using this denomination of "signal" for this beam even for the OPA stage where it rather acts as a pump, and where a second signal at a frequency (f_p–$2f_{MIR}$) is generated.

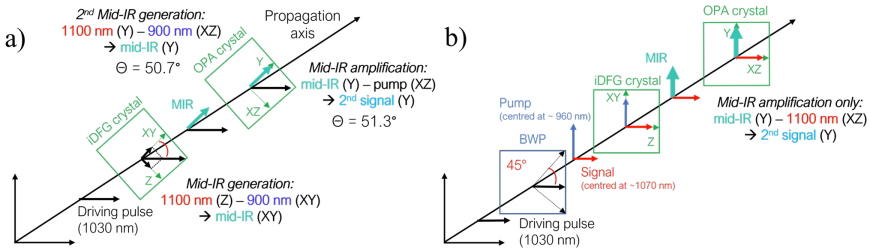

Fig. 14 Sketches of the polarization states along the (a) standard and (b) enhanced iDFG configurations.

During the iDFG stage, the pump spectrum is, of course, depleted, and the signal spectrum is amplified. On the other hand, the signal pulse duration is increased by a factor of approximately 6 due to GVD in LGS, resulting in a reduced input intensity of approximately 20 GW/cm^2 onto the OPA subsequent stage. Consequently, beam size readjustment is important for the OPA stage. Moreover, it is worth noting that depending on the MIR wavelength generated in the iDFG stage, there might be slight differences in the spectra and pulse durations of the signal beam. Because of the signal-to-idler group velocity mismatch (GVM) in the iDFG stage, a certain temporal delay must also be compensated prior to the OPA stage. It needs to be adjusted while tuning the MIR frequency because the GVM is wavelength dependent. The experimental implementation relies on the separation of the signal and MIR beams using a dichroic mirror, which are then independently focused onto the OPA LGS with a temporal synchronization achieved using a delay stage as shown in Fig. 15.

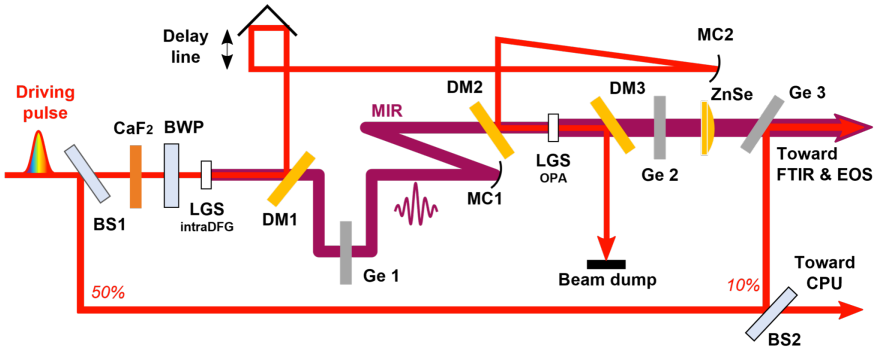

Fig. 15 Schematic of the experimental setup. BS: beamsplitter; BWP: bichromatic waveplate; DM: dichroic mirror (HR for $\lambda < 2$ μm, HT for $\lambda > 2$ μm); MC: curved mirror; CPU: chirped-pulse upconversion.

On the MIR path, a germanium plate is used to temporally compress the pulses prior to the amplification stage. Following the previous EOS measurements 7 mm of Ge are inserted when generating at 8 μm, while the plate is removed when generating at 4.7 μm. Another antireflection-coated (for 900-1100nm with R<1% and for 4-8

μm with R<4%) LGS OPA crystal is used for amplification of the MIR beam. The phase-matching angles are in the XZ plane : θ_{XZ} of 51.5° or 49.8° for 8 and 4.7 μm, respectively, and ϕ_{XZ} of 0°. This corresponds to phase matching for the signal at 1100 nm polarized along the XZ plane and the idler MIR beam along the Y-direction. Concave enhanced silver mirrors are used between the iDFG and OPA stages to loosely focus the NIR and MIR beams in the OPA crystal. The beam sizes are approximately 600 μm and 700 μm for the signal and MIR, respectively. The incident average power is 11.8 W for the pump and signal. Depending on the central wavelength of the MIR, 75% to 87% of the MIR power (from short to long wavelengths) is transmitted between the output of the iDFG crystal and the input of the OPA crystal. As previously mentioned, due to the GDD of 300 fs^2 in the iDFG crystal, the calculated signal pulse duration after the generation stage is approximately 80 fs, corresponding to a peak intensity of approximately 415 GW/cm^2. However, this high intensity associated with the whole energy of the driving pulse at 1 μm (pump and signal) is overestimated, as it was calculated assuming a perfectly Gaussian pulse shape. A better approximation can be done considering the energy contained in the main signal pulse, which was estimated to be 85%, leading to an intensity of approximately 350 GW/cm^2 and the absence of any damage after hours of operation. For comparison, similar intensities have already been reported in experiments [19]. The last part of the setup is similar to the iDFG one: the NIR beam is filtered out using a dichroic mirror, the chirp of the amplified MIR pulse is adjusted with an additional Ge plate, and the beam is collimated by a coated ZnSe lens. To tune the MIR spectrum, we slightly adjust the phase-matching angle ϕ_{XY} of the iDFG crystal while monitoring the MIR central wavelength on the FTIR. Then, we adjust the phase-matching angle θ_{XZ} of the OPA crystal while monitoring the MIR spectrum with the FTIR. When the highest spectral density (corresponding to the highest amplification gain) is reached at the same central wavelength previously generated, we fix θ_{XZ}. During the amplification process, a second signal beam is generated with a wavelength ranging from 1600 to 1275 nm, depending on the central wavelength of the MIR. As its wavelength is closer to the NIR signal than the MIR one, its power is higher than the power added to the MIR beam. In the experiments that follow, we have thoroughly verified that it is being filtered by the DM3 of Fig. 15. For instance, Fig. 16 (a) displays the reflected spectrum (using a NIRQuest-512-1.9, Ocean Optics) for an amplification at 4.7 μm, illustrating at the same time the generation of the second signal. The spectral tunability at the iDFG and OPA stages for a 1 mm-thick iDFG crystal and a 3 mm-thick OPA crystal are measured with our home-built FTIR spectrometer and shown in Fig. 16 (b).

The MIR spectrum is tunable over a bandwidth extending from 3.5 to 8 μm, still covering a range of more than one octave in the MIR. At short MIR wavelengths, the amplified bandwidth for each spectrum is not reduced compared to the iDFG stage. It is even observed to be slightly increased for the one centered at 4.7 μm. Specifically, the bandwidth is measured at 300 cm^{-1} compared to 200 cm^{-1} at -10 dB, corresponding to an FTL pulsed duration of 80 fs instead of 132 fs. This is due to the amplification of the weak band generated around 5.2 μm at the output of the iDFG stage in this particular case. For the long-wavelength range, the amplified spectral width is significantly reduced, and the FTL pulsed duration increases from 47 to 86

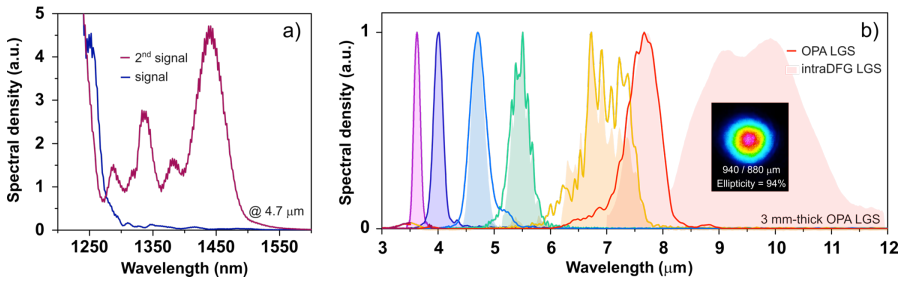

Fig. 16 (a) Edge of the signal spectrum after the iDFG crystal (blue curve) and 2nd signal spectrum generated during the amplification of the MIR pulse centered at 4.7 μm (red curve). (b) Measured tunability of the MIR spectrum at the output of the iDFG in a 1 mm-thick LGS (filled curves) and adding a 3 mm-thick OPA LGS crystal (solid curves). Inset: spatial profile of the amplified 4.7 μm beam.

fs. We attribute this behavior to the very different GVD-induced temporal broadening between the 8 μm MIR and signal pulses. Indeed, the GVD values are 4000 fs^2/mm and 250 fs^2/mm for the MIR and signal, respectively. As a consequence, after a 1 mm propagation, the signal is more than a factor of 2 shorter than the MIR pulse, thereby limiting the amplifier spectral bandwidth. The output spatial profile at 4.7 μm is shown in the insets of Fig. 16 (b). The collimated beam size is $\sim$ 900 μm and shows a Gaussian shape with a corresponding ellipticity of 94%. The pulses have also been experimentally measured using the EOS technique and Fig. 17 and Fig. 18 show EOS traces of the amplified output both around 8 μm and 4.7 μm respectively.

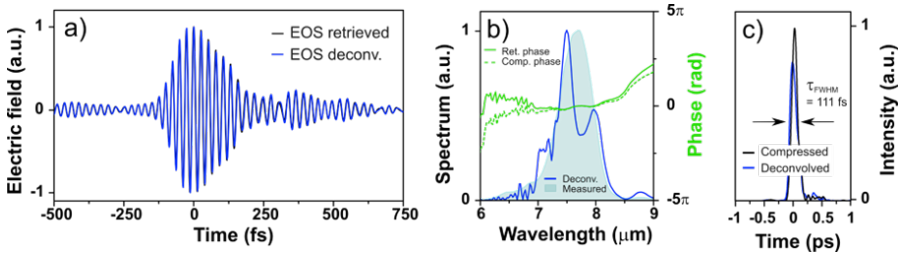

Fig. 17 (a) Raw (black curve) and deconvolved (blue curve) time-domain EOS traces for a 3 mm-thick OPA crystal at 8 μm. (b) Fourier transforms of the EOS time-domain traces. The retrieved spectral phase (green curve), the one corresponding to the compressed pulse (green dashed line), and the spectrum measured with the FTIR spectrometer (gray filled curve) are also shown. (c) Corresponding intensity profiles in the time domain.

The measured amplified powers, shown in Fig. 19 (a), range between 10 to 223 mW, corresponding to energy values of 40 to 890 nJ. This leads to gains ranging from 3.3 to 10.3 from 3.5 μm to 8 μm, with the highest gain of 12 achieved at 7 μm. Taking into account the Fresnel losses at the interfaces of the LGS, ZnSe DM, and Ge plate, the total optical-to-optical efficiencies range between 0.08 and 1.8%, with a quantum efficiency of $\sim$ 14.5% for the latter. Note that this value is calculated with the total incident driving power (with both the pump and signal photons). The lower gains are due to higher GVM in the OPA crystal between the shortest MIR wavelengths

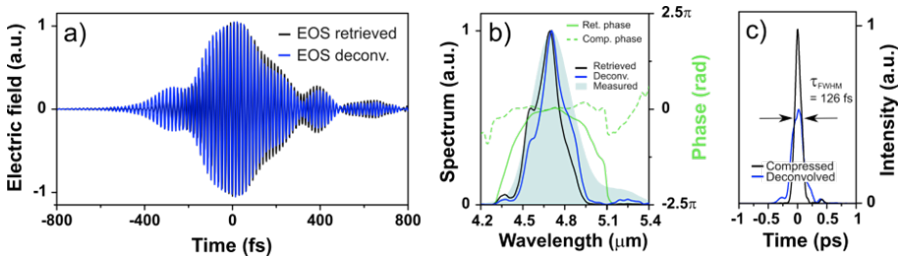

Fig. 18 (a) Raw (black curve) and deconvolved (blue curve) time-domain EOS traces for a 3 mm-thick OPA crystal at 4.7 μm. (b) Fourier transforms of the EOS time-domain traces. The retrieved spectral phase (green curve), the one corresponding to the compressed pulse (green dashed line), and the spectrum measured with the FTIR spectrometer (gray filled curve) are also shown. (c) Corresponding intensity profiles in the time domain.

and the signal pulses, which also seems to be observed for wavelengths higher than 7.5 μm. This effect is demonstrated by several measurements using OPA crystals of different thicknesses at 4.7 μm (see Fig. 19 (b)): the energy increases with thickness until reaching a maximum of 340 nJ (gain = 9.3) for a 3 mm-thick crystal, which corresponds to an optical efficiency of 0.7%.

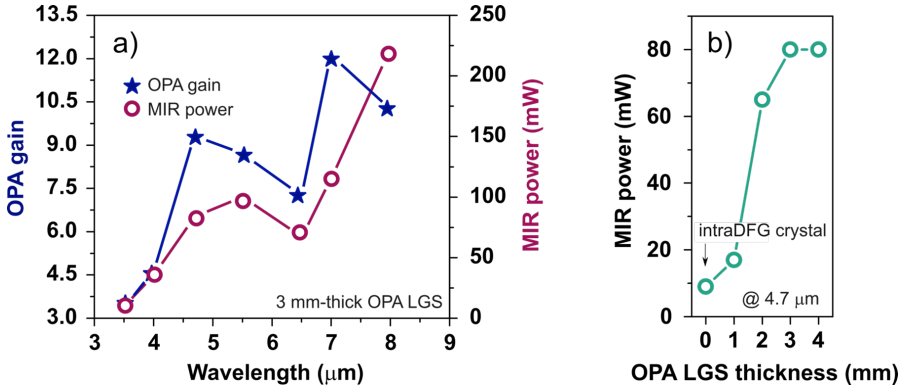

Fig. 19 (a) OPA gain (blue stars) and amplified MIR average powers (purple circle). (b) Measured output amplified MIR average powers at 4.7 μm as a function of the OPA LGS thickness. The 0 mm thickness corresponds to no OPA signal at the output of the 1 mm-thick iDFG crystal.

The OPA architecture we just described is very convenient for studying the amplification process powered by the recycled signal photons, as it allows for a high degree of freedom over several parameters. However, this iDFG technique hides a bonus advantage. Indeed, it easily permits further optical parametric amplification in an all-inline configuration. Because of the use of a BWP and an iDFG crystal phase-matched in the XY plane, the amplified signal and MIR beams are orthogonally polarized. As for the enhanced iDFG, a birefringent plate can therefore be used as a time-delay crystal for time synchronization prior to the OPA stage, giving the opportunity of the straightforward in-line configuration. This implementation is described in details in [44], and results in efficiencies that are very similar to those reported here.

6 Conclusion

In this paper, we address the efficiency issues of iDFG systems in the purpose of generating high-energy mid-infrared (MIR) pulses typically between 4 and 10 μm. We highlight two techniques to improve this efficiency up to two orders of magnitude. First, a shaping of the driving pulse is proposed to enhance efficiency, involving optimizations in the generation process using birefringent multi-order waveplate (BWP), pulse chirp pre-compensation, and delay adjustments. Combining these techniques, the gain of a 2-mm-thick LGS crystal is increased by a factor up to 5, achieving efficiencies ranging from 0.1% to 0.5% at estimated intensities of 120 GW/cm^2. This approach enables to reach efficiencies similar to those seen in 1 μm-pumped OPA-based configurations and nearly on par with those achieved in iDFG architectures pumped at 2 μm. Further efficiency improvement is achieved by recycling the iDFG signal - whose photon number has been increased during the process- to pump a subsequent OPA stage. This architecture allowed a high degree of freedom on several key parameters, which can be independently adjusted, such as beam focusing, continuous delay variation, and chirp adjustment. We measured gain above 3 and up to 12, depending on the central MIR wavelength, leading to a MIR pulse efficiency of 1.8% at 8 μm. The broadband spectral tunability over more than one octave is conserved. This amplification stage can be implemented in an all-inline geometry, resulting in an efficient, versatile, low-noise [45] and compact MIR ultrafast source. At last, the results developed in this manuscript can be extended to crystals other than LGS, and different pump wavelengths, to potentially overcome the conversion efficiency limitations typically associated to iDFG.

Acknowledgments. We gratefully acknowledge the financial support provided by the Agence Nationale de la Recherche (ANR) through the projects ANR MIRTHYX (Grant ID: ANR-19-CE30-0001-MIRTHYX) and the Labex PALM (Grant ID: ANR-10-LABX-0039-PALM).

References

[1] Ghimire, S., DiChiara, A.D., Sistrunk, E., Agostini, P., DiMauro, L.F., Reis, D.A.: Observation of high-order harmonic generation in a bulk crystal. Nature physics **7**(2), 138–141 (2011)

[2] Dombi, P., Pápa, Z., Vogelsang, J., Yalunin, S.V., Sivis, M., Herink, G., Schäfer, S., Groß, P., Ropers, C., Lienau, C.: Strong-field nano-optics. Reviews of Modern Physics **92**(2), 025003 (2020)

[3] Pupeza, I., Huber, M., Trubetskov, M., Schweinberger, W., Hussain, S.A., Hofer, C., Fritsch, K., Poetzlberger, M., Vamos, L., Fill, E., *et al.*: Field-resolved infrared spectroscopy of biological systems. Nature **577**(7788), 52–59 (2020)

[4] Ogilvie, J.P., Kubarych, K.J.: Multidimensional electronic and vibrational spectroscopy: An ultrafast probe of molecular relaxation and reaction dynamics. Advances In Atomic, Molecular, and Optical Physics **57**, 249–321 (2009)

[5] Hamm, P., Zanni, M.: Concepts and Methods of 2D Infrared Spectroscopy. Cambridge University Press, ??? (2011)

[6] Petti, M.K., Lomont, J.P., Maj, M., Zanni, M.T.: Two-dimensional spectroscopy is being used to address core scientific questions in biology and materials science. The Journal of Physical Chemistry B **122**(6), 1771–1780 (2018)

[7] Luther, B.M., Tracy, K.M., Gerrity, M., Brown, S., Krummel, A.T.: 2d ir spectroscopy at 100 khz utilizing a mid-ir opcpa laser source. Optics express **24**(4), 4117–4127 (2016)

[8] Donaldson, P., Greetham, G., Shaw, D., Parker, A., Towrie, M.: A 100 khz pulse shaping 2d-ir spectrometer based on dual yb: Kgw amplifiers. The Journal of Physical Chemistry A **122**(3), 780–787 (2018)

[9] Fritzsch, R., Donaldson, P.M., Greetham, G.M., Towrie, M., Parker, A.W., Baker, M.J., Hunt, N.T.: Rapid screening of dna–ligand complexes via 2d-ir spectroscopy and anova–pca. Analytical chemistry **90**(4), 2732–2740 (2018)

[10] Seidel, M., Xiao, X., Hussain, S.A., Arisholm, G., Hartung, A., Zawilski, K.T., Schunemann, P.G., Habel, F., Trubetskov, M., Pervak, V., *et al.*: Multi-watt, multi-octave, mid-infrared femtosecond source. Science advances **4**(4), 1526 (2018)

[11] Penwell, S.B., Whaley-Mayda, L., Tokmakoff, A.: Single-stage mhz mid-ir opa using ligas 2 and a fiber laser pump source. Optics letters **43**(6), 1363–1366 (2018)

[12] Heiner, Z., Petrov, V., Mero, M.: Efficient, sub-4-cycle, 1-μm-pumped optical parametric amplifier at 10 μm based on baga 4 s 7. Optics Letters **45**(20), 5692–5695 (2020)

[13] Budriūnas, R., Jurkus, K., Vengris, M., Varanavičius, A.: Long seed, short pump: converting yb-doped laser radiation to multi-μj few-cycle pulses tunable through 2.5–15 μm. Optics express **30**(8), 13009–13023 (2022)

[14] Chen, B.-H., Wittmann, E., Morimoto, Y., Baum, P., Riedle, E.: Octave-spanning single-cycle middle-infrared generation through optical parametric amplification in ligas 2. Optics Express **27**(15), 21306–21318 (2019)

[15] Qu, S., Liang, H., Liu, K., Zou, X., Li, W., Wang, Q.J., Zhang, Y.: 9 μm few-cycle optical parametric chirped-pulse amplifier based on ligas 2. Optics letters **44**(10), 2422–2425 (2019)

[16] Heiner, Z., Petrov, V., Panyutin, V.L., Badikov, V.V., Kato, K., Miyata, K., Mero, M.: Efficient generation of few-cycle pulses beyond 10 μm from an optical parametric amplifier pumped by a 1-μm laser system. Scientific Reports **12**(1), 5082 (2022)

[17] Bonvalet, A., Joffre, M., Martin, J., Migus, A.: Generation of ultrabroadband femtosecond pulses in the mid-infrared by optical rectification of 15 fs light pulses at 100 mhz repetition rate. Applied Physics Letters **67**(20), 2907–2909 (1995)

[18] Kaindl, R., Smith, D., Joschko, M., Hasselbeck, M., Woerner, M., Elsaesser, T.: Femtosecond infrared pulses tunable from 9 to 18?? μm at an 88-mhz repetition rate. Optics letters **23**(11), 861–863 (1998)

[19] Pupeza, I., Sánchez, D., Zhang, J., Lilienfein, N., Seidel, M., Karpowicz, N., Paasch-Colberg, T., Znakovskaya, I., Pescher, M., Schweinberger, W., *et al.*: High-power sub-two-cycle mid-infrared pulses at 100 mhz repetition rate. Nature Photonics **9**(11), 721–724 (2015)

[20] Chen, B.-H., Nagy, T., Baum, P.: Efficient middle-infrared generation in ligas 2 by simultaneous spectral broadening and difference-frequency generation. Optics Letters **43**(8), 1742–1745 (2018)

[21] Liu, J., Ma, J., Lu, D., Gu, X., Cui, Z., Yuan, P., Wang, J., Xie, G., Yu, H., Zhang, H., *et al.*: Few-cycle pulses tunable from 3 to 7 μm via intrapulse difference-frequency generation in oxide lgn crystals. Optics Letters **45**(20), 5728–5731 (2020)

[22] Weigel, A., Jacob, P., Gröters, D., Buberl, T., Huber, M., Trubetskov, M., Heberle, J., Pupeza, I.: Ultra-rapid electro-optic sampling of octave-spanning mid-infrared waveforms. Optics Express **29**(13), 20747–20764 (2021)

[23] Kanda, N., Ishii, N., Itatani, J., Matsunaga, R.: Optical parametric amplification of phase-stable terahertz-to-mid-infrared pulses studied in the time domain. Optics Express **29**(3), 3479–3489 (2021)

[24] Wang, Q., Zhang, J., Kessel, A., Nagl, N., Pervak, V., Pronin, O., Mak, K.F.: Broadband mid-infrared coverage (2–17 μm) with few-cycle pulses via cascaded parametric processes. Optics Letters **44**(10), 2566–2569 (2019)

[25] Nakamura, T., Badarla, V.R., Hashimoto, K., Schunemann, P.G., Ideguchi, T.: Simple approach to broadband mid-infrared pulse generation with a mode-locked yb-doped fiber laser. Optics Letters **47**(7), 1790–1793 (2022)

[26] Kowligy, A.S., Timmers, H., Lind, A.J., Karlen, S., Cruz, F., Schunemann, P.G., Biegert, J., Diddams, S.A.: Near-single-cycle long-wave infrared pulses for coherent linear and nonlinear optics. In: CLEO: Science and Innovations, pp. 4–5 (2019). Optica Publishing Group

[27] Novák, O., Krogen, P.R., Kroh, T., Mocek, T., Kärtner, F.X., Hong, K.-H.: Femtosecond 8.5 μm source based on intrapulse difference-frequency generation of 2.1 μm pulses. Optics letters **43**(6), 1335–1338 (2018)

[28] Gaida, C., Gebhardt, M., Heuermann, T., Stutzki, F., Jauregui, C., Antonio-Lopez, J., Schülzgen, A., Amezcua-Correa, R., Tünnermann, A., Pupeza, I., *et al.*: Watt-scale super-octave mid-infrared intrapulse difference frequency generation. Light: Science & Applications **7**(1), 94 (2018)

[29] Butler, T., Gerz, D., Hofer, C., Xu, J., Gaida, C., Heuermann, T., Gebhardt, M., Vamos, L., Schweinberger, W., Gessner, J., *et al.*: Watt-scale 50-mhz source of single-cycle waveform-stable pulses in the molecular fingerprint region. Optics letters **44**(7), 1730–1733 (2019)

[30] Vasilyev, S., Moskalev, I.S., Smolski, V.O., Peppers, J.M., Mirov, M., Muraviev, A.V., Zawilski, K., Schunemann, P.G., Mirov, S.B., Vodopyanov, K.L., *et al.*: Super-octave longwave mid-infrared coherent transients produced by optical rectification of few-cycle 2.5-μm pulses. Optica **6**(1), 111–114 (2019)

[31] Zhang, J., Wang, Q., Hao, J., Liu, H., Yao, J., Li, Z., Liu, J., Mak, K.F.: Broadband, few-cycle mid-infrared continuum based on the intra-pulse difference frequency generation with bgse crystals. Optics Express **28**(25), 37903–37909 (2020)

[32] Liu, K., Liang, H., Qu, S., Li, W., Zou, X., Zhang, Y., Wang, Q.J.: High-energy mid-infrared intrapulse difference-frequency generation with 5.3% conversion efficiency driven at 3 μm. Optics Express **27**(26), 37706–37713 (2019)

[33] Steinleitner, P., Nagl, N., Kowalczyk, M., Zhang, J., Pervak, V., Hofer, C., Hudzikowski, A., Sotor, J., Weigel, A., Krausz, F., *et al.*: Single-cycle infrared waveform control. Nature Photonics **16**(7), 512–518 (2022)

[34] Kassab, H., Gröbmeyer, S., Schweinberger, W., Hofer, C., Steinleitner, P., Högner, M., Amotchkina, T., Gerz, D., Knorr, M., Huber, R., *et al.*: In-line synthesis of multi-octave phase-stable infrared light. Optics Express **31**(15), 24862–24874 (2023)

[35] Lavenu, L., Natile, M., Guichard, F., Délen, X., Hanna, M., Zaouter, Y., Georges, P.: High-power two-cycle ultrafast source based on hybrid nonlinear compression. Optics express **27**(3), 1958–1967 (2019)

[36] Kubarych, K.J., Joffre, M., Moore, A., Belabas, N., Jonas, D.M.: Mid-infrared electric field characterization using a visible charge-coupled-device-based spectrometer. Optics letters **30**(10), 1228–1230 (2005)

[37] Wang, W., Wu, H., Liu, C., Sun, B., Liang, H.: Multigigawatt 50 fs yb: Calgo regenerative amplifier system with 11 w average power and mid-infrared generation. Photonics Research **9**(8), 1439–1445 (2021)

[38] Huber, R., Brodschelm, A., Tauser, F., Leitenstorfer, A.: Generation and field-resolved detection of femtosecond electromagnetic pulses tunable up to 41 thz.

Applied Physics Letters **76**(22), 3191–3193 (2000)

[39] Bournet, Q., Guichard, F., Natile, M., Zaouter, Y., Joffre, M., Bonvalet, A., Pupeza, I., Hofer, C., Druon, F., Hanna, M., Georges, P.: Enhanced intrapulse difference frequency generation in the mid-infrared by a spectrally dependent polarization state. Opt. Lett. **47**(2), 261–264 (2022)

[40] Miranda, M., Fordell, T., Arnold, C., L'Huillier, A., Crespo, H.: Simultaneous compression and characterization of ultrashort laser pulses using chirped mirrors and glass wedges. Optics express **20**(1), 688–697 (2012)

[41] Bromage, J., Rothhardt, J., Hädrich, S., Dorrer, C., Jocher, C., Demmler, S., Limpert, J., Tünnermann, A., Zuegel, J.: Analysis and suppression of parasitic processes in noncollinear optical parametric amplifiers. Optics Express **19**(18), 16797–16808 (2011)

[42] Manzoni, C., Först, M., Ehrke, H., Cavalleri, A.: Single-shot detection and direct control of carrier phase drift of midinfrared pulses. Opt. Lett. **35**(5), 757–759 (2010)

[43] Yamakawa, T., Sono, N., Kitao, T., Morimoto, T., Kida, N., Miyamoto, T., Okamoto, H.: Long-term stabilization of carrier envelope phases of mid-infrared pulses for the precise detection of phase-sensitive responses to electromagnetic waves. AIP Advances **10**(2), 025311 (2020)

[44] Bournet, Q., Jonusas, M., Zheng, A., Guichard, F., Natile, M., Zaouter, Y., Joffre, M., Bonvalet, A., Druon, F., Hanna, M., Georges, P.: Inline amplification of mid-infrared intrapulse difference frequency generation. Opt. Lett. **47**(19), 4885–4888 (2022)

[45] Bournet, Q., Natile, M., Jonusas, M., Guichard, F., Zaouter, Y., Joffre, M., Bonvalet, A., Druon, F., Hanna, M., Georges, P.: Intensity noise in difference frequency generation-based tunable femtosecond mir sources. Opt. Express **31**(8), 12693–12702 (2023)